Extended level structure of ^{51}Cr with measured mean lifetimes of yrast states in agreement with shell-model calculations

R. Chakrabarti [1,*] S. Mukhopadhyay [2,3,†] B. V. John,[2,3] D. C. Biswas [2,3] S. K. Tandel [4] L. S. Danu,[2] Y. K. Gupta,[2,3] B. N. Joshi,[2] G. K. Prajapati,[2] S. Saha [5] J. Sethi,[5] and R. Palit[5]

[1]*Department of Physics, University of Mumbai, Vidyanagari, Mumbai 400098, India*
[2]*Nuclear Physics Division, Bhabha Atomic Research Centre, Mumbai 400085, India*
[3]*Homi Bhabha National Institute, Anushaktinagar, Mumbai 400094, India*
[4]*Department of Physics, Shiv Nadar Institution of Eminence, Delhi-NCR 201314, India*
[5]*Department of Nuclear and Atomic Physics, Tata Institute of Fundamental Research, Mumbai 400005, India*

An investigation using the ^{27}Al(^{28}Si, $3p1n$) reaction and the high-efficiency Indian National Gamma Array has yielded an enriched level scheme for the ^{51}Cr nucleus. Multiple new γ rays, including high-energy feeders to the yrast states, have been observed. The yrast $K^{\pi} = \frac{15}{2}^{-}$ three-quasiparticle band structure has been extended beyond band termination. Angular correlation and polarization measurements have yielded unambiguous spins and parities to most of the observed yrast states. Unambiguous measurements of mean lifetimes for the yrast states in the $K^{\pi} = \frac{15}{2}^{-}$ band, leading to and even beyond band termination, have been carried out for the first time in this nucleus. This, coupled with the clear identifications of weak intraband crossover transitions, have facilitated profiling of the evolution of $B(E2)$ values along the yrast sequence. Large-scale shell model calculations in the full fp valence space, with no restriction on the occupancy of the valence orbitals, have been performed. The results from such calculations have been found to be consistent with the experimental observations.

I. INTRODUCTION

Nuclei in the $A \approx 50$ mass region have neutron and proton numbers between 20 and 28. Thus, their ground-state configuration is predominantly $(f_{7/2})^n$, and hence these nuclei are often referred to as $f_{7/2}$-shell nuclei. Among these, nuclei which have nucleon numbers near shell closure are likely to exhibit single-particle structures, whereas the midshell nuclei have distinct collective behavior [1]. Overall, the feature that is commonly observed in the nuclear level schemes in this mass region is the coexistence of both these structures in the same nucleus, which allows us to study the interplay between the single-particle and collective modes of nuclear excitations. The result of this interplay is evident in the observation of many interesting phenomena, such as backbending, band termination, and shape change [2].

The ^{51}Cr nucleus, with 24 protons and 27 neutrons has the $\pi f_{7/2}^4 \nu f_{7/2}^{-1}$ configuration in its ground state. Apparently, the half-filled $(f_{7/2})^n$ proton orbital drives this nucleus toward a deformed shape, and the neutron-hole configuration, which is one short of the magic number 28, pushes it toward sphericity. This unique underlying configuration results in band structures with varying levels of deformation. Four such bands

were reported from previous investigations with bandheads at $K^{\pi} = \frac{1}{2}^{-}$, $\frac{7}{2}^{-}$, $\frac{3}{2}^{-}$, and $\frac{15}{2}^{-}$ [3,4]. Initially, based on the measured electromagnetic properties of the low-lying levels, only $K^{\pi} = \frac{1}{2}^{-}$ and $\frac{7}{2}^{-}$ bands were identified by Szoghy *et al.* [5]. The $K^{\pi} = \frac{1}{2}^{-}$ band was later confirmed by Kasagi and Onhuma [6]. The spins and parities of the member states belonging to these two bands were confirmed by angular distribution and linear polarization measurements by Sawa *et al.* [7] and Kasagi *et al.* [8]. The bandlike structure built on $K^{\pi} = \frac{3}{2}^{-}$ at $E_x = 1899$ keV was first observed by Avasthi *et al.* [9]. All of the above results came through $(p, n\gamma)$ or $(\alpha, n\gamma)$ reactions. The latest experimental investigation of ^{51}Cr using heavy-ion-induced reaction was carried out by Cameron *et al.* [2]. In this measurement, both ^{40}Ca(^{14}N, $3p$)^{51}Cr and ^{27}Al(^{27}Al, $2pn$)^{51}Cr reactions were used, and an array of up to five Ge detectors and a NaI multiplicity filter was employed to detect the emitted γ rays. Following subsequent analysis, the high-spin band was extended beyond the maximum spin allowed within the $f_{\frac{7}{2}}$ shell, i.e., the band-terminating state. However, there are several questions that have remained unanswered in the level structure of ^{51}Cr. The data on the states beyond band termination were inadequate. The weak crossover $E2$ transitions, connecting the yrast states and leading to the band-terminating state, remained unobserved. The mean lifetimes of the yrast states in the $K^{\pi} = \frac{15}{2}^{-}$ structure, derived from the attenuation of Doppler shifts, were mostly effective lifetimes. Unobserved fast side-feeds to the yrast states

———
*ritwika.chakrabarti@gmail.com; Previously at Nuclear Physics Division, Bhabha Atomic Research Centre, Mumbai 400085, India.
†somm@barc.gov.in, somsundarm@gmail.com

were invoked to explain certain effective lifetimes. The large uncertainties in the reported lifetimes were also attributed to these "unknown" side-feedings. However, these anticipated fast side-feeds have remained unobserved in the past three decades.

The present investigation aims to address all these unanswered questions and ambiguities. Although most of the fp-shell nuclei were thoroughly investigated employing heavy-ion reactions and high-efficiency detector arrays over the past few decades, new information on the level scheme of ^{51}Cr nucleus has remained elusive since the heavy-ion work by Cameron *et al.* [2]. This may be due to the unfavored population of nonyrast states in a chosen heavy-ion reaction or even owing to the smearing out of the fast as well as weak high-energy transitions due to large recoil velocity.

In this paper, an enriched level scheme of the ^{51}Cr nucleus is reported following a dedicated investigation using heavy-ion-induced reaction that has not been done since the early 1990s. Apart from extending the yrast structure beyond band termination, angular correlation and polarization measurements have been carried out to assign the spins and parities of almost all the observed yrast states. The mean lifetimes of states up to and even beyond the band-terminating state have been unambiguously measured for the first time in this nucleus. The long-anticipated, unknown, side-feeding transitions to the yrast states in the $K^{\pi} = \frac{15}{2}^{-}$ band have now been clearly identified. New calculations under the framework of shell model with a large basis have been performed, and the results have been found to be in excellent agreement with the experimental observables.

II. EXPERIMENTAL DETAILS

The experiment was carried out at the Pelletron-Linac facility, Tata Institute of Fundamental Research (TIFR), Mumbai. Excited states in the ^{51}Cr nucleus were populated using the ^{27}Al(^{28}Si, $3p1n$) reaction at a beam energy of 100 MeV. The target was a $\approx$750-μg/cm^2-thick Al foil, backed by a 14.8-mg/cm^2-thick layer of Au in order to slow down and ultimately stop the recoiling nuclei within the thickness of the backing material. Coincidence events with fold-2 and above were recorded employing the Indian National Gamma Array (INGA) spectrometer. During the measurement, INGA was composed of 20 Compton-suppressed high-purity clover Ge detectors, of which 4 were at 90°, 2 each at 23° and 115°, and 3 each at 40°, 65°, 140°, and 157° with respect to the beam direction. Data were acquired using a digital data acquisition system [10] that employed Pixie-16 modules from XIA-LLC, USA. The data, thus acquired, were analyzed offline using the RADWARE suite of software and LINESHAPE analysis code [11–14].

III. DATA ANALYSIS AND RESULTS

In the offline analysis, the acquired data were sorted into conventional symmetric γ-γ matrix and and three-dimensional γ^3 cube. The relative intensities and branching ratios of the observed transitions in ^{51}Cr were measured by taking the data recorded by all detectors in the array into account. Spins and parities for the excited nuclear levels have
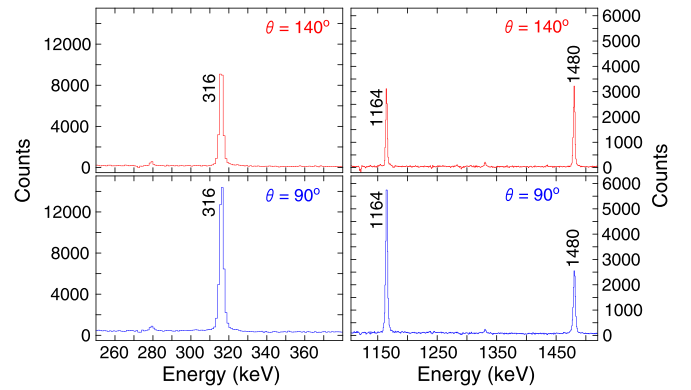
FIG. 1. Quality of energy-gated spectra observed in detectors at 140° (90°), with energy-gate on a stretched quadrupole transition (775 keV), recorded in the detectors placed at 90° (140°). The R_{DCO} values have been found to be consistent with the previously assigned multipolarities to such known transitions, as depicted in the figure.

been determined following angular correlation and linear polarization measurements using different types of asymmetric γ-γ matrices. Asymmetric (angle dependent) γ-γ matrices, with data recorded at 90° vs forward angle detectors, as well as 90° vs complementary backward angle detectors, with respect to the beam direction, were also constructed to generate gated projection of γ rays at different angles for LINESHAPE analysis.

A. Determination of spin and parity

The spin assignments of the observed excited states were made from the measured directional correlation of γ-rays deexciting oriented states (DCO) ratios [15]. This method is based on the observed coincidence intensity anisotropy, obtained from the angle dependent γ-γ coincidences. The DCO ratio in the present work was defined as

$$R_{\mathrm{DCO}} = \frac{I_{\gamma 1}(\text{at } 140° \text{ gated by } \gamma_2 \text{ at } 90°)}{I_{\gamma 1}(\text{at } 90° \text{ gated by } \gamma_2 \text{ at } 140°)}. \quad (1)$$

Thus from Eq. (1), the DCO ratio of a γ transition (γ_1) of unknown multipolarity was obtained from the ratio of its intensities at two angles, viz., 140° and 90° when the energy gate is on another transition (γ_2) of known multipolarity. The intensities were extracted from an asymmetric, angle-dependent γ-γ matrix, where the energies deposited in detectors at 90° were plotted along one axis, and along the other axis, coincidence events detected in detectors at 140° were plotted. The gating transition in all cases was always a stretched $E2$. Figures 1 and 2 are the representative spectra obtained by setting energy gates on the x and y axes of the asymmetric DCO matrix in which some of the transitions of known as well as unknown multipolarities belonging to ^{51}Cr are visible. The spectra in Figs. 1 and 2 clearly reveal the difference in intensities of the coincident γ transition at the two angles. The R_{DCO} values for transitions in ^{51}Cr obtained from such spectra are listed in Table I and pictorially represented in Fig. 3. R_{DCO} values of several transitions of known multipolarities belonging to ^{49}V, ^{46}Ti, and ^{51}Mn nuclei

TABLE I. The excitation energies of the levels, transition energies, spins, and parities of the corresponding initial and final levels; relative intensities of the γ transitions; DCO ratios (R_{DCO}); polarization asymmetries (Δ_{asymm}); and assigned multipolarities in ^{51}Cr. Only those levels and γ transitions that have been observed in the present work are tabulated. Spin-parity and multipolarity assignments from present work are indicated in the footnotes. The rest are from Ref. [3].

E_x[a] (keV)	E_γ (keV)	$J_i^\pi \to J_f^\pi$	I_γ (%)	R_{DCO}	Δ_{asymm}	Multipolarity
749.1(3)	749.1(3)	$\frac{3}{2}^- \to \frac{7}{2}^-_1$	1.0(3)			$E2$
777.0(4)						
1164.52(9)	1164.5(1)	$\frac{9}{2}^-_1 \to \frac{7}{2}^-_1$	57.3(22)			$M1+E2$
1353.4(4)	576.4(4)	$\frac{5}{2}^- \to \frac{1}{2}^-$				$E2$
	604.3(3)	$\frac{5}{2}^- \to \frac{3}{2}^-$				$M1+E2$
1480.12(9)	315.6(1)	$\frac{11}{2}^{-\,b}_1 \to \frac{9}{2}^-_1$	58.4(20)	0.64(2)	$-0.07(1)$	$M1+E2$[b]
	1480.1(1)	$\frac{11}{2}^{-\,b}_1 \to \frac{7}{2}^-_1$	66.2(27)	1.03(2)	0.04(1)	$E2$[b]
1557.8(4)	204.4(3)	$\frac{7}{2}^-_2 \to \frac{5}{2}^-$				$[M1]$
	808.7(3)	$\frac{7}{2}^-_2 \to \frac{3}{2}^-$				$E2$[b]
2255.53(13)	775.4(1)	$\frac{15}{2}^{-\,b}_1 \to \frac{11}{2}^{-\,b}_1$	100.0	0.99(2)	0.06(1)	$E2$
2380.1(5)	822.3(4)	$\frac{9}{2}^-_2 \to \frac{7}{2}^-_2$				$M1+E2$
	1026.7(4)	$\frac{9}{2}^-_2 \to \frac{5}{2}^-$				$E2$
2385.4(4)	905.3(3)	$\frac{13}{2}^- \to \frac{11}{2}^{-\,b}_1$				$M1+E2$
2704.7(5)	1146.9(3)	$\frac{11}{2}^- \to \frac{7}{2}^-_2$				$E2$
3181.14(16)	925.6(1)	$\frac{17}{2}^{-\,b}_1 \to \frac{15}{2}^{-\,b}_1$	83.2(33)	0.50(2)	$-0.06(1)$	$M1+E2$[b]
3367.2(5)	981.8 (3)	$(\frac{15}{2}^-_2)^{c,\,d} \to \frac{13}{2}^-$				$(M1+E2)$[f]
3818.05(18)	636.9(1)	$\frac{19}{2}^{-\,b}_1 \to \frac{17}{2}^{-\,b}_1$	64.2(34)	0.52(2)	$-0.06(1)$	$M1+E2$[b]
	1562.5(2)	$\frac{19}{2}^{-\,b}_1 \to \frac{15}{2}^{-\,b}_1$	3.4(5)			$(E2)$[f]
3995.5(6)	1290.8(3)	$(\frac{15}{2}^-_3)^{c,\,d} \to \frac{11}{2}^-_2$				$(E2)$[f]
4489.6(4)	2234.0(3)	$(\frac{17}{2})^{-\,c,\,e}_2 \to \frac{15}{2}^{-\,b}_1$	2.4(5)		$-0.08(1)$	$(M1+E2)$[f]
5472.9(3)	1654.8(4)	$(\frac{19}{2}^-_2)^c \to \frac{19}{2}^{-\,b}_1$				$(M1+E2)$[f]
	2291.7(3)	$(\frac{19}{2}^-_2)^c \to \frac{17}{2}^{-\,b}_1$				$(M1+E2)$[f]
5564.47(21)	1746.4(2)	$\frac{21}{2}^{-\,b} \to \frac{19}{2}^{-\,b}_1$	6.4(4)	0.56(4)	$-0.05(1)$	$M1+E2$[b]
	2383.3(3)	$\frac{21}{2}^{-\,b} \to \frac{17}{2}^{-\,b}_1$	1.8(3)			$(E2)$[f]
5714.08(20)	149.6(2)	$\frac{23}{2}^{-\,b}_1 \to \frac{21}{2}^{-\,b}$	1.8(3)			$(M1+E2)$[f]
	1896.0(1)	$\frac{23}{2}^{-\,b}_1 \to \frac{19}{2}^{-\,b}_1$	46.9(24)	0.95(4)	0.06(1)	$E2$[b]
6894.97(25)	1330.5(2)	$(\frac{23}{2})^{-\,c,\,e}_2 \to \frac{21}{2}^{-\,b}$	2.9(4)		$-0.18(2)$	$(M1+E2)$[f]
	1422.0(4)	$(\frac{23}{2})^{-\,c,\,e}_2 \to (\frac{19}{2}^-_2)^c$				$(E2)$[f]
	3076.8(4)	$(\frac{23}{2})^{-\,c,\,e}_2 \to \frac{19}{2}^{-\,b}_1$				$(E2)$[f]
8491.8(4)	2777.6(3)	$(\frac{25}{2})^{-\,c,\,e}_1 \to \frac{23}{2}^{-\,b}_1$	7.7(17)		$-0.10(1)$	$(M1+E2)$[f]
8515.9(4)	1620.9(3)	$(\frac{25}{2}^-_2)^c \to (\frac{23}{2})^{-\,c,\,e}_2$				$(M1+E2)$[f]
	2801.7(4)	$(\frac{25}{2}^-_2)^c \to \frac{23}{2}^{-\,b}_1$				$(M1+E2)$[f]
9299.1(4)	807.3(2)	$(\frac{27}{2})^{-\,c,\,e}_1 \to (\frac{25}{2})^{-\,c,\,e}_1$	6.9(14)		$-0.13(2)$	$(M1+E2)$[f]
	3584.9(5)	$(\frac{27}{2})^{-\,c,\,e}_1 \to \frac{23}{2}^{-\,b}_1$				$(E2)$[f]

[a]Level energies (E_x) and their uncertainties are obtained by making least-squares fits to the γ-ray energies (E_γ) using the Gamma TO Level program [16].
[b]Unambiguous assignment following DCO and polarization measurements in present work.
[c]From shell-model calculations in present work.
[d]Following systematics in neighboring isotope(see text).
[e]Parity assignment from polarization measurements.
[f]Most probable assignment from present work.
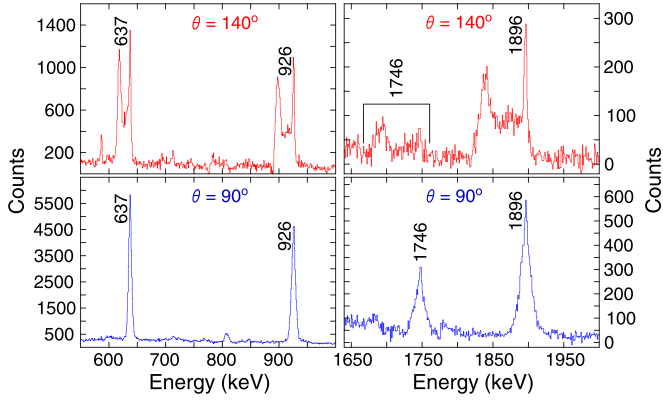
FIG. 2. Representative energy-gated spectra observed in detectors at 140° (90°), with energy gate on a stretched quadrupole transition (775 keV), recorded in the detectors placed at 90° (140°). The R_{DCO} values for the 637-, 926-, 1746-, and 1896-keV γ rays, extracted using these spectra, are listed in Table I along with their unambiguously assigned multipolarities.

populated in the present experiment have also been plotted in Fig. 3 for reference. The weighted mean of the R_{DCO} values of known quadrupole transitions came out to be 0.99(1) and that for the predominantly dipole transitions comes out to be 0.53(1), when the gate is on a stretched $E2$ transition. Two dotted lines corresponding to $\Delta J = 2$ and $\Delta J = 1$ have been drawn through the above-mentioned weighted mean values, respectively, to guide the eye. These were taken as the typical values or reference values for determining the multipolarities of unknown transitions.

The parity of the excited states were determined from the linear polarization asymmetry which is defined as [17,18]:

$$\Delta_{\text{asymm}} = \frac{aN_\perp - N_\parallel}{aN_\perp + N_\parallel}, \qquad (2)$$

where $N_\perp$ and $N_\parallel$ are the number of photons with a given energy scattered along the direction perpendicular and parallel
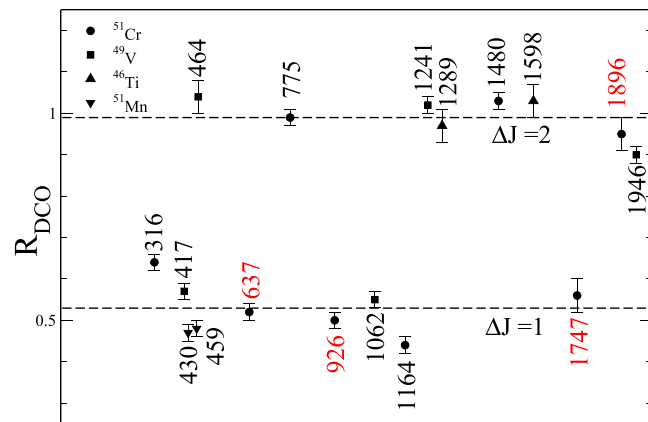
FIG. 3. The R_{DCO} values determined in the present work for transitions in ^{51}Cr, ^{49}V, ^{46}Ti, and ^{51}Mn from different quadrupole energy gates. The transitions with previously known and newly determined multipolarities are denoted with black and red, respectively. The $\Delta J = 1$ and $\Delta J = 2$ lines are drawn to guide the eye (see text for details).
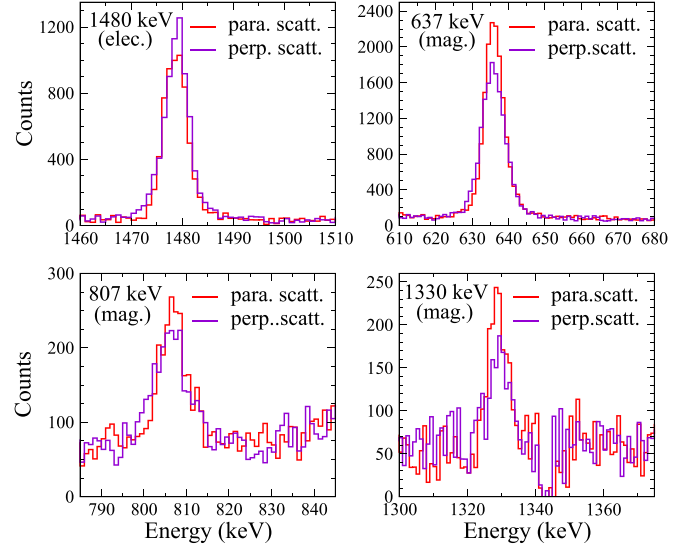
FIG. 4. Representative perpendicular and parallel scattered spectra observed in 90° detectors. The photopeak counts of the perpendicular and parallel scattered events indicate that the 1480-keV γ ray is dominantly electric, whereas the 637-, 807-, and 1330-keV γ rays are of dominantly magnetic nature.

to the reaction plane, respectively, in the detectors placed at $\approx 90°$ and in coincidence with another photon detected in at least one other detector in the array. These were obtained from two asymmetric matrices with one axis corresponding to perpendicular or parallel scattered events recorded by clovers at 90° and the other axis corresponding to the total energy recorded in any of the other detectors. The asymmetry between the perpendicular and parallel scattering with respect to the reaction plane distinguishes between electric and magnetic transitions. "a" denotes the geometrical correction factor of the array due to the asymmetry in the response of the clover segments. This factor is energy dependent ($a = a_0 + a_1 E_\gamma$) and is determined using a radioactive source (having no spin alignment) under similar conditions. This correction factor is defined as

$$a = \frac{N_\parallel(\text{unpolarized})}{N_\perp(\text{unpolarized})}. \qquad (3)$$

In the present work a_0 was found to be 0.96584(344) and a_1 was found to be $(1.48126 \pm 0.60231) \times 10^{-5}$ keV^{-1}; a_1 being negligibly small was not considered in the calculations. An electric transition (magnetic transition) will undergo more perpendicular scattering (parallel scattering) than parallel scattering (perpendicular scattering) and give a positive (negative) Δ_{asymm} value. Figures 4 and 5 elucidate the identification of electric/magnetic nature of γ transitions through this method. The Δ_{asymm} values for all the transitions in ^{51}Cr determined in present work are listed in Table I and plotted in Fig. 5. The Δ_{asymm} value for some transitions in ^{49}V, ^{46}Ti, and ^{51}Mn of known electric/magnetic nature are also plotted in Fig. 5 for reference.
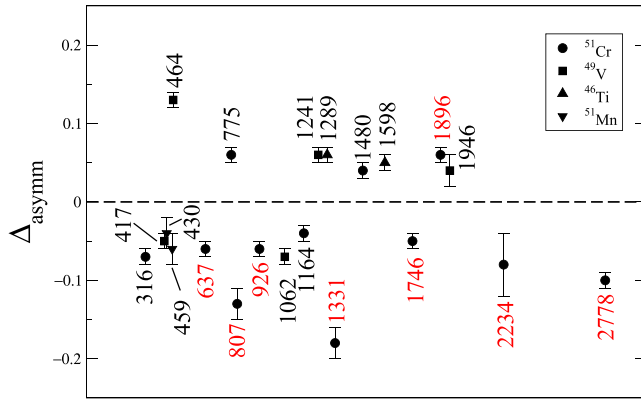
FIG. 5. Plot of the Δ_{asymm} values, as determined in the present work for the transitions in ^{51}Cr, ^{49}V, ^{46}Ti, and ^{51}Mn. The γ transitions of known electromagnetic nature are denoted in black, whereas the newly determined ones are shown in red. The dotted line through zero value of Δ_{asymm} has been drawn to guide the eye.

B. Level scheme

Following the observation of multiple new transitions, and their placement based on coincidence relationship and inten-sity arguments, the level scheme of ^{51}Cr nucleus has now been significantly extended with respect to the earlier reported work [2]. The level scheme, as developed from the present data, is depicted in Fig. 6. The transitions are listed in Table I along with their relative intensities, R_{DCO}, and polarization asymmetry values that were determined in the present work. It is to be noted that only the transitions observed in the current data set have been shown in Fig. 6 and listed in Table I. The relative intensities for a few weak transitions in Table I could not be unambiguously measured due to lack of statistics. Moreover, in certain instances of weak, high-energy transitions, the peak shapes were found to be smeared out due to Doppler broadening and/or shift. The multipolarity assignments from the present work as well as from Ref. [3] are also compiled in Table I.

The previously reported $K^{\pi} = \frac{7}{2}^{-}$ ground-state band, $K^{\pi} = \frac{1}{2}^{-}$ strongly deformed band, and $K^{\pi} = \frac{15}{2}^{-}$ three-quasiparticle band [4] have been observed in the present work (Figs. 6). It is worth noting that this is the first observation of the deformed $K^{\pi} = \frac{1}{2}^{-}$ band structure employing a heavy-ion-induced reaction. In earlier observations, the $K^{\pi} = \frac{1}{2}^{-}$ band was pop-ulated only by employing (p, n) and (α, n) reactions [6,8,9]
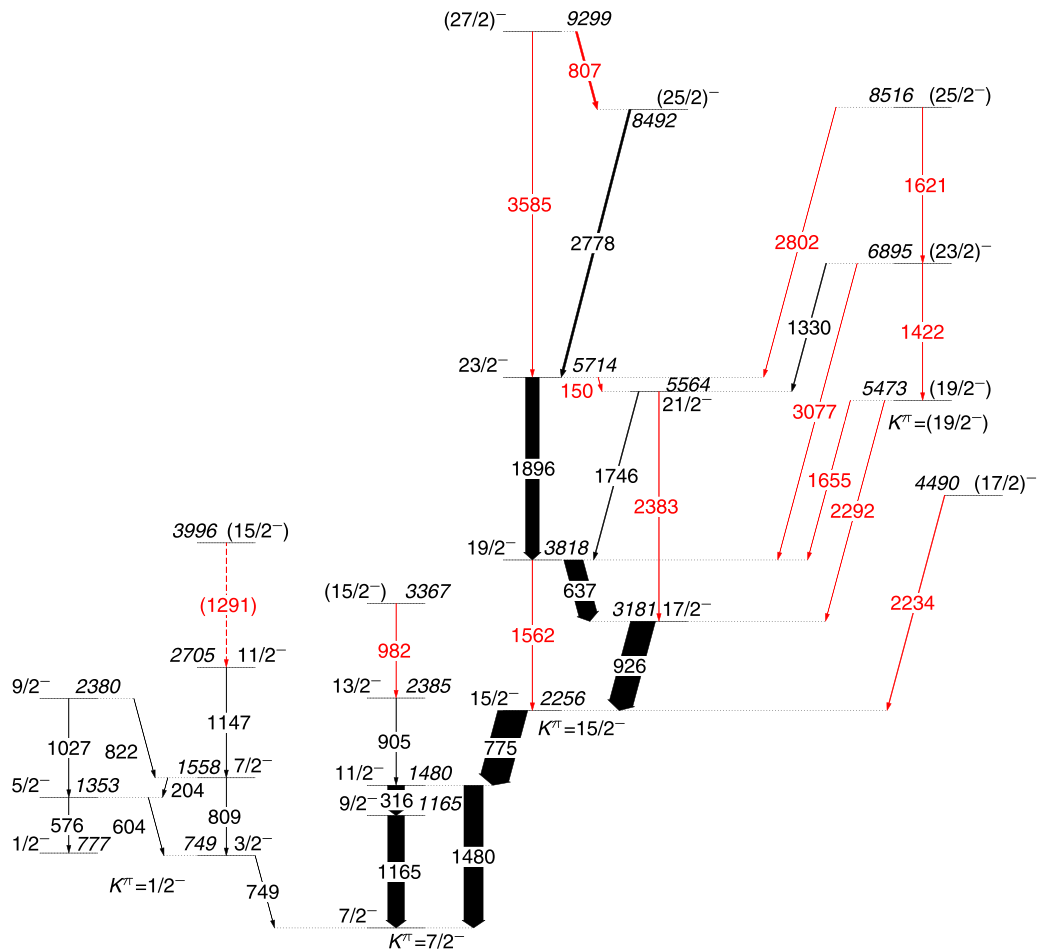
FIG. 6. Partial level scheme of ^{51}Cr, as obtained from the data in the present measurement. The newly observed transitions are shown in red. Spin-parities in parentheses are tentative.
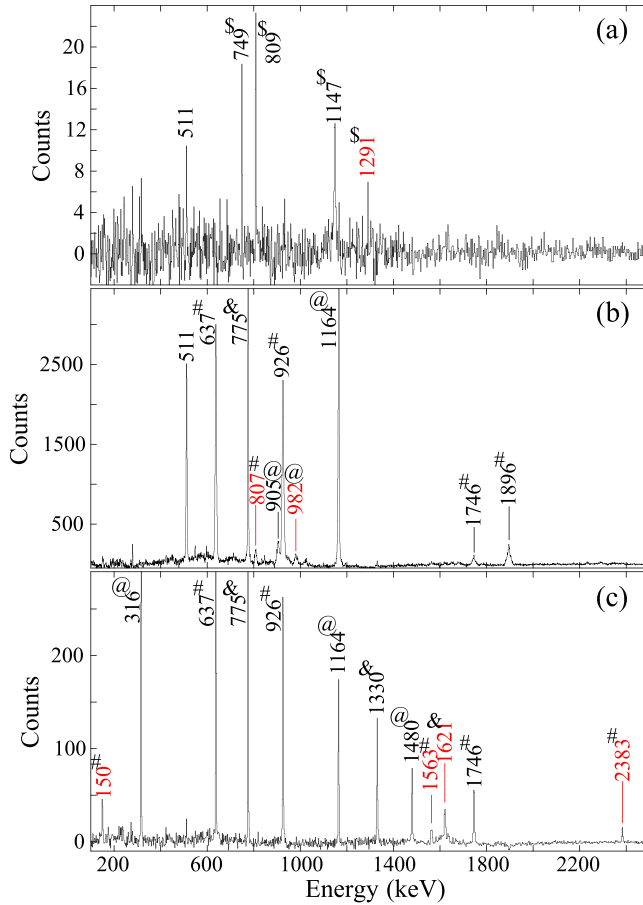
FIG. 7. (a) Sum spectrum of double coincidences using the energy gates 749, 809, and 1147 keV of ^{51}Cr, generated from the γ-γ-γ coincidence events, showing the transitions in the $K^\pi = \frac{1}{2}^-$ strongly deformed band ($) , including the possibly new 1291-keV transition; (b) 316-keV gated spectrum generated from 90° vs 90° symmetric γ-γ matrix, showing transitions from the $K^\pi = \frac{7}{2}^-$ band (@) including the newly observed 982-keV transition and $K^\pi = \frac{15}{2}^-$ band(#) including the newly observed 807-keV transition and others (&); (c) sum spectrum of double coincidences (where double coincidences are generated by considering one transition from the set of γ rays that include 1165, 316, 1481, 775 keV, and the other transition from the set of γ rays that contain 1746, 1331, 1621, 3078 keV) showing several transitions from the $K^\pi = \frac{7}{2}^-$ band (@), $K^\pi = \frac{15}{2}^-$ band (#), and others (&). The newly observed transitions in all three panels are shown in red.

and was observed up to spin, $J^\pi = \frac{11}{2}^-$ ($E_x = 2705$ keV). In the present work, the $K^\pi = \frac{1}{2}^-$ band has been extended tentatively up to spin $J^\pi = (\frac{15}{2}^-)$ ($E_x = 3996$ keV) following the new observation of the 1291-keV transition that feeds the 2705-keV ($J^\pi = \frac{11}{2}^-$) level [Figs. 6 and 7(a)]. Since the 1291-keV transition could be only observed in the sum of double coincidence spectrum with gates on the 749-, 808-, and 1147-keV γ rays [Fig. 7(a)], it has been treated as tentative in the level scheme. The present reaction mechanism populated this band very weakly and the intensities of the transitions could not be extracted. Also they were not intense enough
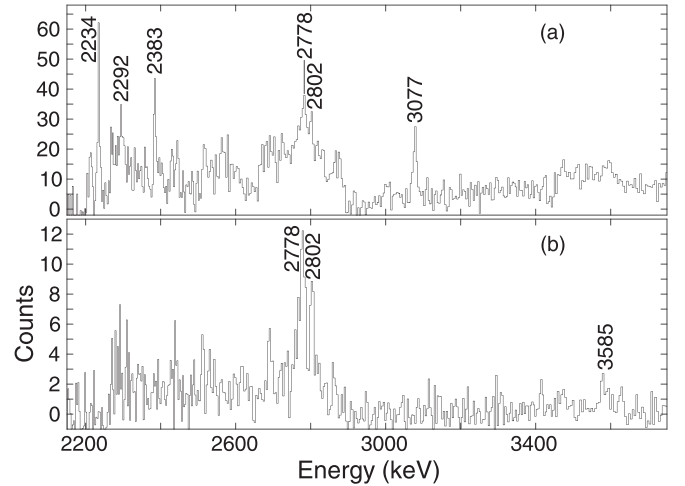
FIG. 8. Representative gated spectra showing high-energy γ rays (above 2 MeV) in ^{51}Cr: (a) Sum of double-energy gates (non diagonal) on transitions in a list containing 1164-, 316-, 775-, 926- and 637-keV γ rays; (b) sum of double-energy gates on 1896 keV, and one from the list containing 1164-, 316-, 1480-, 775-, 926-, and 637-keV γ rays.

for the DCO and polarization measurements to be carried out. The bandhead at the $E_x = 777$ keV, $J^\pi = \frac{1}{2}^-$ level has been reported to decay by a 28-keV γ transition to the 749 keV, $J^\pi = \frac{3}{2}^-$ level by Saha *et al.* [19]. We could not observe this low-energy transition due to a higher cut-off set in the electronics signal threshold. A direct decay of the 777-keV level to the ground state has not been observed in any of the previous works [3] and no such transition was observed in the present data either.

With the new observation of the 982-keV transition, the $K^\pi = \frac{7}{2}^-$ band has now been extended to the excitation energy, $E_x = 3367$ keV [Figs. 6 and 7(b)]. The $K^\pi = \frac{15}{2}^-$ three-quasiparticle band decays out to the ground band through the strong 775-keV $E2$ transition only. The weak crossover transitions of energies 1562 keV ($\frac{19}{2}^-_1 \rightarrow \frac{15}{2}^-_1$) and 2383 keV ($\frac{21}{2}^-_1 \rightarrow \frac{17}{2}^-_1$), along with the 150 keV that connects the band-terminating, $\frac{23}{2}^-$, and the yrast $\frac{21}{2}^-$ states, have been newly observed (Fig. 6). Beyond band termination, Cameron *et al.* [2] reported a state with $E_x = 8485$ keV and a tentatively assigned spin $(\frac{25}{2}, \frac{27}{2}^-)$ [2]. In the present data, the excitation energy of this state has been unambiguously fixed at 8492 keV, which deexcites by a fast-emitting 2778 keV (not 2774 keV as reported in Ref. [2]) transition, feeding the $\frac{23}{2}^-_1$ band-terminating state. A new γ transition of energy 807 keV, feeding this $(\frac{25}{2})^-$ level at $E_x = 8492$ keV, has further extended the level scheme to an excitation energy, $E_x = 9299$ keV. The observation of the crossover 3585-keV transition, although weak, has affirmed the excitation energy of this level, which is the highest experimentally observed one in this nucleus to date. Several of these newly observed transitions are visible in the representative spectra depicted in Figs. 7 and 8 with different gating conditions. The DCO and polarization measurements have allowed us to unambiguously

assign the spin and parity to the states belonging to the $K^\pi = \frac{15}{2}^-$ band up to the band termination for the first time (Table I). Beyond this, the polarization measurements confirmed the parity of the $E_x = 8492$ and 9299 keV as negative. However, due to the low intensity and the Doppler broadening of the deexciting transitions, the spins could not be experimentally determined through the DCO method.

Apart from these bands, seven other new transitions, viz., 1422, 1621, 1655, 2234, 2292, 2802, and 3077 keV, that do not belong to any of the above-mentioned bands, have been observed in the present data. Among these, all the transitions except the first two (i.e., 1422 and 1621 keV), have been found to feed the $K^\pi = \frac{15}{2}^-$ three-quasiparticle band. Coincidence analysis using γ^3 cube has further revealed that the 1422- and 1621-keV transitions possibly constitute the $K^\pi = (\frac{19}{2}^-)$ (see Sec. IV) band in this nucleus, with the 1331-, 1655-, 2292-, 2802-, and 3077-keV transitions connecting the states of the newly proposed $K^\pi = (\frac{19}{2}^-)$ sequence to the yrast states in the $K^\pi = \frac{15}{2}^-$ three-quasiparticle bands. The intensity of the transitions belonging to this proposed band were too weak to be extracted and DCO and polarization measurements were also not possible. However, we could extract the polarization asymmetry values of the 1331-keV transition that allowed the assignment of negative parity to the $E_x = 6895$-keV level.

C. Lifetime measurement

One of the primary aims of the present investigation was to unambiguously measure the mean lifetimes of the excited states in the $K^\pi = \frac{15}{2}^-$ three-quasiparticle band up to the band-terminating state and beyond. Distinct Doppler-broadened line shapes were observed in the forward and backward angle detectors for the 926-, 637-, 1746-, 1896-, and 2778-keV transitions, deexciting the yrast $\frac{17}{2}^-$, $\frac{19}{2}^-$, $\frac{21}{2}^-$, $\frac{23}{2}^-$, and $(\frac{25}{2})^-$ states, respectively, in the $K^\pi = \frac{15}{2}^-$ band [20].

Energy-gated spectra, projected on the forward, transverse, and complementary backward angles, were used to extract the mean lifetimes of the yrast levels of the $K^\pi = \frac{15}{2}^-$ band. The spectra with the energy gate on 775-keV transition were mostly used to fit the Doppler-broadened line shapes. In instances where there were insufficient counts under the peak and its Doppler-broadened regions, spectra with energy gates on 775 keV, and the stopped-transitions below the yrast $\frac{11}{2}^-$ states, were summed together for each angle to enhance the statistics of coincidence events.

The LINESHAPE analysis package from Wells and Johnson was used for the lifetime analysis [13,14]. The analysis, considering three angles at a time, was mostly done using spectra projected on $65°$, $90°$, and $115°$ angles. However, for all the transitions except 1746 and 2778 keV, data from other subset of angles (viz. $40°$, $90°$, and $140°$) were also analyzed, and the results between the two subset of angles were found to be in good agreement within experimental uncertainties. A total of 10 000 Monte Carlo simulations of velocity history of the recoiling nuclei traversing the target (Al) and backing material (Au) were generated in time steps of 0.0001 ps. Electronic stopping powers were calculated following the heavy-ion stopping power theory by Ziegler *et al.* [21]. More

details about the multiple steps that are involved in the fitting procedures of Doppler-broadened shapes of γ transitions can be found in Ref. [22]. The quality of Doppler-broadened spectra with DSAM fits to the data are shown in Figs. 9 and 10, and the mean lifetimes of the levels, as obtained following this analysis, are summarized in Table II. Uncertainties in the lifetime values were determined from the behavior of χ^2-fit in the vicinity of the minimum. However, the systematic error that is associated with the modeling of the stopping power, and which can be as large as 10–15%, is not included in the quoted errors (Table II). The mean lifetime (τ) of the newly observed yrast $(\frac{25}{2})^-$ level has been extracted for the first time in the present work. A value of $\tau = 0.11(3)$ ps has been measured for this level, which is in excellent agreement with the one that has been obtained from shell-model calculations ($\tau_{th} = 0.13$ ps). An effective lifetime of 1.7 ps was proposed earlier for the yrast $\frac{23}{2}^-$ band-terminating state by Cameron *et al.* [2]. In the present measurement, the mean lifetime value of $\tau = 0.42(5)$ ps has been obtained for this state. No attempt was made earlier to measure the mean lifetime of the yrast 5564-keV, $\frac{21}{2}^-$ level, which, prior to the present work, was found to be fed by only a sharp 1331-keV γ ray and depopulated by only a weak 1746-keV γ transition [2]. Now, with the additional new information on the feeding (and decay) transitions of (from) this level, the mean lifetime of this yrast $\frac{21}{2}^-$ level was measured to be $\tau = 0.07(1)$ ps by fitting the 1746 keV (relative intensity $\approx$6% with respect to 775 keV) γ transition for the first time (Fig. 10). For the yrast $\frac{19}{2}^-$ level, an effective lifetime of 0.4 ps was reported earlier, whereas a mean lifetime of 0.6 ps, with an estimated uncertainty of about $\approx$30–50% due to unknown side-feeding, was assigned to the yrast $\frac{17}{2}^-$ level [2]. In the present work, a mean lifetime of 0.31(3) ps was obtained for the yrast $\frac{19}{2}^-$ state. For the yrast $\frac{17}{2}^-$ level, an unambiguous mean lifetime value of $\tau = 0.08(2)$ ps was obtained by fitting the spectra generated by gating-from-above (GFA), thus completely avoiding the uncertainty that arises due to unknown side-feeding (Fig. 10).

The reduced $M1$ and $E2$ transition probabilities for the yrast states were deduced using the experimental mean lifetimes and tabulated in Table II along with the corresponding calculated values from the shell model. It is to be noted that the quoted errors in the experimental reduced transition probabilities include the errors associated with transition energies. The electromagnetic properties of the yrast states up to band termination were further studied through the deduction of the electric quadrupole moment and the g factors. The values obtained are listed in Table III. The body-fixed (intrinsic) electric quadrupole moment (Q_0) was deduced from the measured $B(E2)$ values for the $K^\pi = \frac{7}{2}^-$ and the $K^\pi = \frac{15}{2}^-$ yrast structures using the relation

$$B(E2; I_i \to I_f) = \frac{5}{16\pi} Q_0^2 \langle I_i K_i 0 | I_f K_f \rangle^2, \qquad (4)$$

where I is the spin and K is the projection of the spin on the symmetry axis. This is based on the assumption of purely rotational states within a rotational band where neither K nor
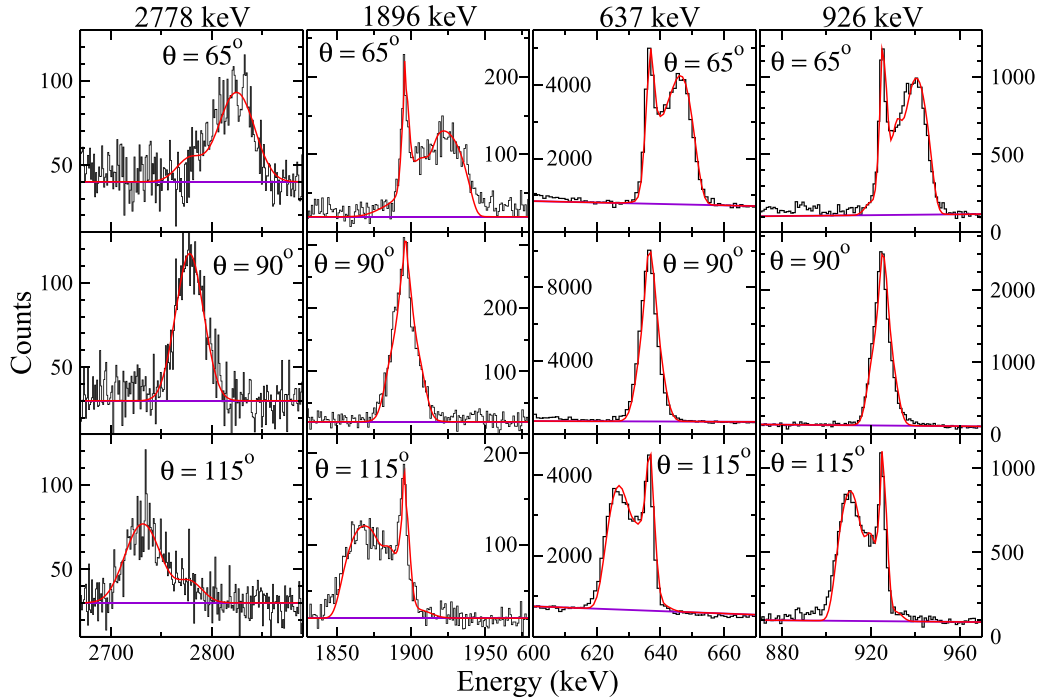
FIG. 9. Profiles of Doppler-broadened line shapes, generated by gating-from-below (GFB), in forward, transverse, and backward angles, and representative curve fittings using LINESHAPE code for some of the relevant transitions in the $K^\pi = \frac{15}{2}^-$ band [20].

the intrinsic quadrupole moment change [4,23]. The sign of the intrinsic quadrupole moment Q_0 is positive for prolate deformation and negative for oblate deformation. The deformation parameter, β_2, assuming axial deformation is related to Q_0 through the following equation [4]:

$$Q_0 \approx \frac{3}{\sqrt{5}} Z R_0^2 \beta_2 (1 + 0.36\beta_2). \tag{5}$$

FIG. 10. Doppler-broadened line-shape fittings of 926- and 1746-keV γ transitions in forward and backward angles. The spectra for the 926-keV transition in this figure have been extracted by gating-from-above (GFA).

Here deformation is not large and hence $\beta_2^2 \ll 1$. Hence the second term in the Eq. (5) can be ignored and β_2 were obtained using the following equation:

$$Q_0 \approx \frac{3}{\sqrt{5}} Z R_0^2 \beta_2 \tag{6}$$

and are also listed in Table III.

The g factor for a state with spin I and $K \neq 1/2$ was determined using the following relations:

$$g = g_R + (g_K - g_R)\frac{K^2}{I(I+1)}, \tag{7}$$

$$B(M1) = \frac{3}{4\pi} K^2 (g_K - g_R)^2 |\langle I_i K_i 10 | I_f K_f \rangle|^2, \tag{8}$$

where g_R is the contribution resulting from the collective rotational motion of the nucleus ($g_R \approx Z/A$) and g_K is the intrinsic contribution.

Along with the Q_0 and g-factor values deduced from the above-mentioned equations, the corresponding values as obtained from shell-model calculations are also listed in Table III. The empirical g factors (g_{emp}) listed in Table III are discussed in the next section.

IV. THEORETICAL CALCULATIONS AND DISCUSSION

The $K^\pi = \frac{1}{2}^-$, $\frac{7}{2}^-$, and $\frac{15}{2}^-$ bands were earlier explained using shell model and, alternatively, the Nilsson and the particle rotor models [4,5,24]. The $K^\pi = \frac{1}{2}^-$ and $\frac{7}{2}^-$ bands are predicted to be based on $\nu[321]1/2^-$ and $\nu[303]7/2^-$ Nilsson orbitals. The $K^\pi = 15/2^-$ band has been interpreted in the Nilsson model as a three-quasiparticle band, with the $\frac{15}{2}^-$

TABLE II. Lifetimes of the yrast states and the corresponding reduced transition probabilities in ^{51}Cr.

Spin	Level energy	Lifetime		Reduced transition probability			
	E_x	τ		$B(E2)$		$B(M1)$	
$(\hbar)$	(keV)	(ps)		$(e^2\,\text{fm}^4)$		(μ_N^2)	
		Expt.	Theo.[c]	Expt.	Theo.[c]	Expt.	Theo.[c]
$\frac{9}{2}^-_1$	1164.52(9)	0.11(1)[a]	0.08			0.33(3)[a]	0.4
$\frac{11}{2}^-_1$	1480.12(9)	0.79^{+35}_{-6}[a]	1.17	77.2^{+59}_{-336}[a]	82.0	1.07^{+9}_{-48}[a]	1.1
$\frac{15}{2}^-_1$	2255.53(13)	66.1(20)[a]	41.45	44.0(13)[a]	55.8		
$\frac{17}{2}^-_1$	3181.14(16)	0.08(2)[d]	0.08			0.9(2)[b]	0.8
$\frac{19}{2}^-_1$	3818.05(18)	0.31(3)	0.33	14.1(31)	26.4	0.7(1)[b]	0.9
$\frac{21}{2}^-$	5564.47(21)	0.07(1)	0.06	33.3(77)	38.3	0.119(20)[b]	0.112
$\frac{23}{2}^-_1$	5714.08(20)	0.42(5)	0.27	76.1(106)	77.4	1.5(3)[b]	0.8
$(\frac{25}{2}^-)_1$	8491.8(4)	0.11(3)	0.13			0.024(7)[b]	0.022

[a]Reference [3].
[b]Assuming pure $M1$ multipolarity.
[c]From shell-model calculations in present work.
[d]Obtained by GFA.

bandhead formed by raising one proton from [321]3/2$^-$ to [312]5/2$^-$ orbital and coupling of the three unpaired nucleons to the maximum value of K [4]. Pure Nilsson-model calculations were unable to reproduce the energies and the ordering of the levels in both the $K^\pi = \frac{1}{2}^-$ and $K^\pi = \frac{7}{2}^-$ bands, as shown by Szoghy *et al.* [5]. The strong-coupling symmetric rotor model including the Coriolis coupling between bands was used to calculate the negative-parity states in odd-even $1f_{7/2}$ nuclei [24]. This model reproduced the experimental energies and ordering of the $\frac{3}{2}^-$ and $\frac{1}{2}^-$ levels very well in the $K^\pi = \frac{1}{2}^-$ band in ^{51}Cr for $\beta = 0.20$ [25]. The $\frac{5}{2}^-$ and $\frac{7}{2}^-$ levels were also reasonably well reproduced. However, it could not reproduce the spin sequence of the yrast levels that belong to the $K^\pi = \frac{7}{2}^-$ band [6].

Shell-model calculations

The shell-model calculations previously reported for the yrast and nonyrast states in ^{51}Cr were carried out by either allowing the excitation of a maximum of three particles [4] or a maximum of five particles [26] to the levels above $f_{7/2}$.

The present work reports the first-ever large-scale shell-model (LSSM) calculation for all the observed states in the ^{51}Cr nucleus in full fp valence space, with no restrictions on the number of particles that can be excited from the $1f_{7/2}$ orbital to the higher fp orbitals [27]. The calculations have been carried out employing High Performance Computing System at Nuclear Physics Division, BARC. Three effective interactions, i.e., GXPF1A [28], KB3G [29], and FPD6 [30], that have been routinely employed for this mass region, have been used in the code NuShellX [31] for calculating the

TABLE III. Electric quadrupole moments, deformation parameters, and g factors of yrast states up to band termination in ^{51}Cr. The Q_0, β_2, and g-factor values are deduced from experimental reduced transition probabilities (listed in Table II). The corresponding values obtained from shell-model calculations for Q_0 and g factors are also listed. The empirical g factors (g_{emp}) calculated for the states in $K^\pi = \frac{7}{2}^-$ and the $K^\pi = \frac{15}{2}^-$ bands are also tabulated.

Level	Level energy (keV)	Q_0 $(ef\,m^2)$	β_2	$Q_{0(\text{SM})}$ $(ef\,m^2)$	g	g_{SM}	g_{emp}
$K = \frac{7}{2}^-$							
$\frac{9}{2}^-$	1164.52(9)				0.86(4)	0.24	0.07
$\frac{11}{2}^-$	1480.12(9)	103.30^{+2304}_{-365}	0.29^{+6}_{-1}	526.89	0.87^{+10}_{-54}	0.45	0.31
$K = \frac{15}{2}^-$							
$\frac{17}{2}^-$	3181.14(16)				1.03(17)	0.75	0.69
$\frac{19}{2}^-$	3818.05(18)	71.06(757)	0.20(2)	43.25	0.78(6)	0.78	0.76
$\frac{21}{2}^-$	5564.47(21)	73.04(886)	0.20(2)	−20.54	0.56(1)	0.84	0.82
$\frac{23}{2}^-$	5714.08(20)	89.01(622)	0.25(2)	106.86	0.72(16)	0.83	0.87
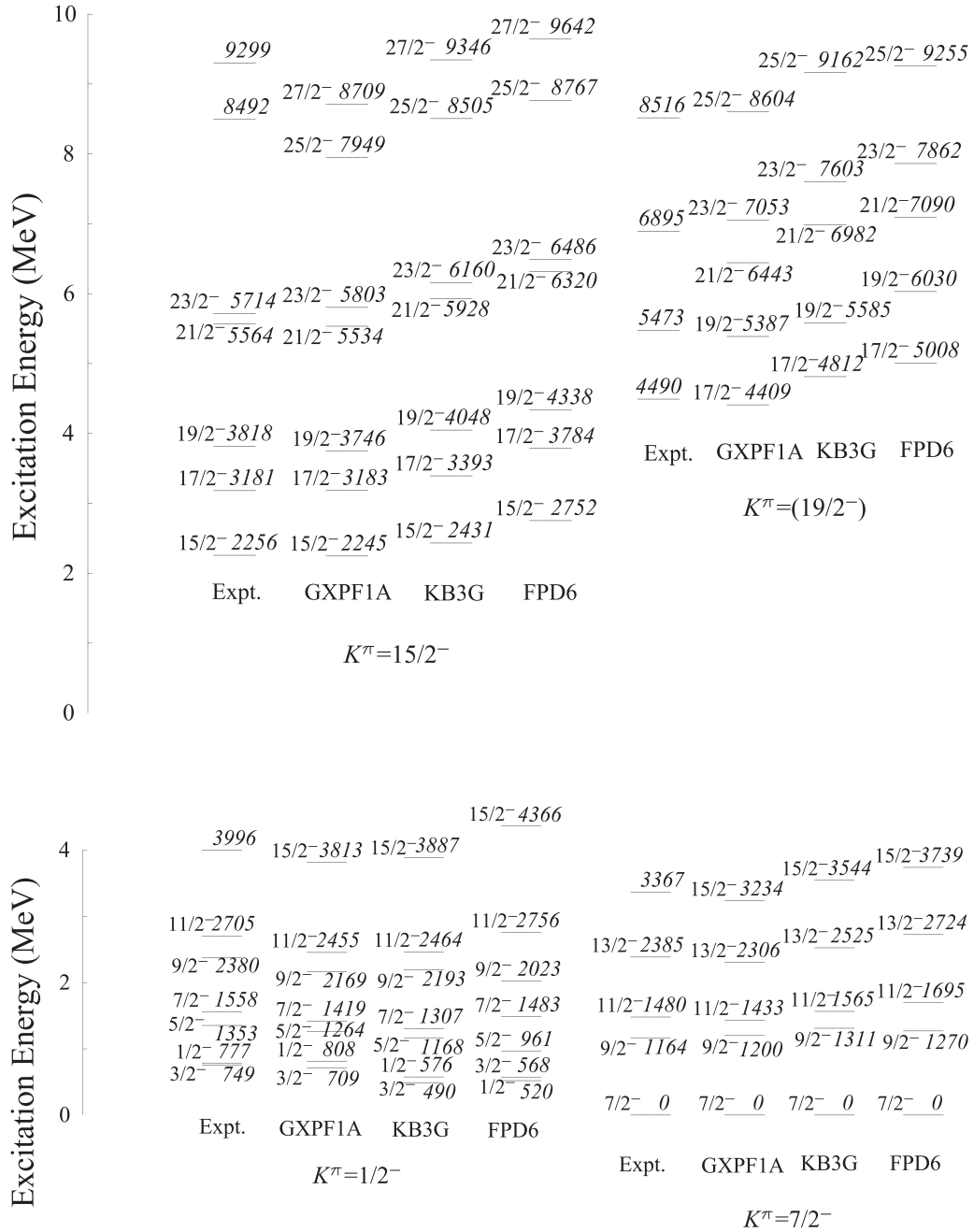
FIG. 11. Comparison between experimentally observed and calculated energy levels in ^{51}Cr.

energy levels, lifetimes, transition probabilities, quadrupole moments, and *g* factors in this nucleus.

The calculated energy levels, using the above-mentioned three interactions, have been compared with the experimental ones in Fig. 11. It is evident that for the levels in the $K^\pi = \frac{1}{2}^-$, $K^\pi = \frac{7}{2}^-$, and $K^\pi = \frac{15}{2}^-$ structures the results are in good agreement. In instances, where unambiguous spin-parity assignments for certain energy levels in the level scheme (Fig. 6) could not be made from experiment, tentative assignments (in parenthesis) have been adopted, guided by the shell-model calculations.

The GXPF1A interaction predicted most of the excitation energies closest to the experimental values. The reduced transition probabilities and the extracted lifetimes were also remarkably well reproduced by the GXPF1A interaction (Table II). Hence, the theoretical calculations discussed hereafter in this paper refers to those done using only the GXPF1A interaction.

The yrast states beyond band termination at 8492 and 9299 keV that were designated negative-parity states from our polarization measurements were predicted to be $\frac{25}{2}^-$ and $\frac{27}{2}^-$ levels, respectively, by the shell model. The newly observed

3367-keV level in the $K^\pi = \frac{7}{2}^-$ band and 3996-keV level in the $K^\pi = \frac{1}{2}^-$ band have been tentatively assigned $J^\pi = (\frac{15}{2}^-_2)$ and $J^\pi = (\frac{15}{2}^-_3)$, respectively, following systematics in neighboring isotope ^{53}Fe [32], as well as predictions from shell-model calculations. The most probable spin-parity assignments for the 5473-, 6895-, and the 8516-keV levels in the proposed $K^\pi = (\frac{19}{2}^-)$ sequence of states, as $(\frac{19}{2}^-)$, $(\frac{23}{2})^-$, and $(\frac{25}{2}^-)$, respectively, are based on the following arguments. The calculations clearly indicate $\frac{19}{2}^-$ and $\frac{25}{2}^-$ spins for the 5473- and 8516-keV levels, respectively. However, the calculations also predict two close-lying energy levels with excitation energies, $E_x = 6443$ keV ($J^\pi = \frac{21}{2}^-$) and 7053 keV ($J^\pi = \frac{23}{2}^-$), and either of them could correspond to the observed 6895-keV level. The mean lifetimes for the $\frac{19}{2}^-_2$ and $\frac{21}{2}^-_2$ levels, as predicted by the shell-model calculations, are almost the same, whereas for the $\frac{23}{2}^-_2$ state, the calculations predict a mean lifetime much longer (viz., five times longer) than that of both the $\frac{19}{2}^-_2$ and $\frac{21}{2}^-_2$ levels. It is observed from the experimental data that the transitions deexciting the 6895-keV level (i.e., 1330- and the newly observed 3077-keV γ rays) are less broadened than the ones that depopulate either the 5473-keV (i.e., 2292-keV γ ray for example) or 8516-keV (i.e., 1621- and 2802-keV γ rays) levels (Figs. 7 and 8). It is worth noting that Cameron *et al.* [2] also observed the 1330.4-keV transition as a narrow line and suggested a lower limit of about 3 ps for the effective lifetime of its originating level ($E_x = 6895$ keV). The above arguments indicate that the 6895-keV level has a longer lifetime than the other two (5473- and 8516-keV) levels. Hence, for the 6895-keV level, $J^\pi = (\frac{23}{2}^-)_2$ has been adopted.

In the present work, the electric quadrupole moments and g factors for the yrast states were also calculated from LSSM and compared with the corresponding experimental values (Table III). The plots of the theoretical values of the intrinsic quadrupole moments, $Q_{0(\text{SM})}$, with spin along the yrast sequence in the $K^\pi = \frac{7}{2}^-$ and $K^\pi = \frac{15}{2}^-$ bands, are depicted in Fig. 12. The signs of the $Q_{0(\text{SM})}$ values indicate a prolate deformation of the yrast states up to band termination at $\frac{23}{2}^-$, with the exception of the $\frac{21}{2}^-$ state, which is picturized as an oblate deformed state under the shell-model framework. The band-terminating state $\frac{23}{2}^-$ where the spins are maximally aligned is a noncollective prolate state [4,33]. These predictions are consistent with the results of previously performed shell-model calculations by Brandolini *et al.* [4]. Shell-model calculations by previous workers for some other nuclei in this mass region, such as ^{51}Mn and ^{52,53}Fe, also indicate a noncollective prolate deformation at the band termination [4]. Interestingly, beyond band termination, the $Q_{0(\text{SM})}$ value turns negative at spin $\frac{27}{2}^-$ in ^{51}Cr, indicating an oblate deformed state.

The dominant neutron and proton configurations for each of the states in the $K^\pi = \frac{15}{2}^-$ band, starting from the bandhead to the band-terminating state and beyond, as predicted by our shell-model calculations, are shown in Table IV. The partitions in which seven neutrons occupy the $\nu f_{7/2}$ orbital, four protons occupy the $\pi f_{7/2}$ orbital, and the rest of the orbitals of
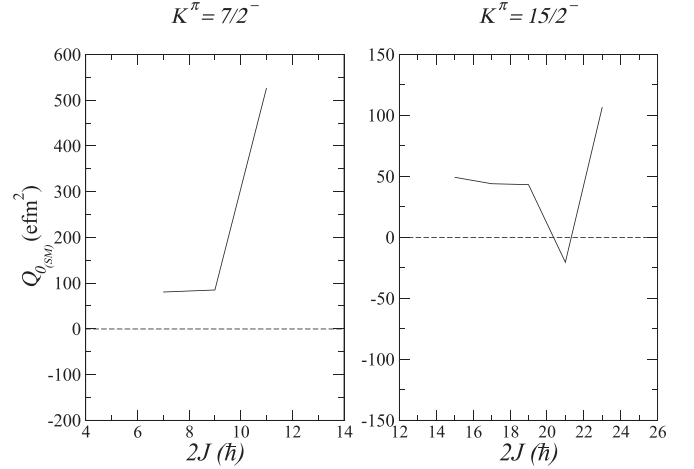
FIG. 12. Variation of deformation along the yrast states in ^{51}Cr in the shell-model framework. Plots of shell-model predicted intrinsic quadrupole moment $Q_{0(\text{SM})}$ with twice the spin (2J) value for the $K^\pi = \frac{7}{2}^-$ and $\frac{15}{2}^-$ bands.

the pf shell have zero occupancy, were found to be the dominant partitions for the yrast states up to band termination. This is essentially the percentage contribution from a pure $(f_{7/2})^{11}$ configuration. Beyond band termination, the above-mentioned pure $f_{7/2}$ neutron and proton configurations remain no longer the dominant partitions for formation of higher-lying states.

From the bandhead to the band termination, the amplitudes of the partitions with $\nu[(f_{7/2})^7 \bigotimes (p_{3/2}p_{1/2}f_{5/2})^0]$ and $\pi[(f_{7/2})^4 \bigotimes (p_{3/2}p_{1/2}f_{5/2})^0]$ configurations increase with spin and attain a maximum at the band termination. This is considered as an indicator of more collectivity at low spins that gradually decreases with increasing spin and becomes minimum as one approaches the band-terminating state. The properties of the band-terminating state are summarized in Table V.

There is an interesting observation to be made here in the context of the present work. The total percentage contribu-

TABLE IV. The dominant neutron and proton configurations for the excites states in $K^\pi = \frac{15}{2}^-$ band as predicted by LSSM. [Neutron partition 1: $(1f_{7/2})^7 \ (2p_{3/2})^0 \ (2p_{1/2})^0 \ (1f_{5/2})^0$. Neutron partition 2: $(1f_{7/2})^6 \ (2p_{3/2})^1 \ (2p_{1/2})^0 \ (1f_{5/2})^0$. Proton partition 1: $(1f_{7/2})^4 \ (2p_{3/2})^0 \ (2p_{1/2})^0 \ (1f_{5/2})^0$.]

				Amplitude (%)	
J^π	E_x (keV)	$2J_n$	$2J_p$	Neutron	Proton
$\frac{15}{2}^-$	2256	7	8	34.62 (partition 1)	40.83 (partition 1)
$\frac{17}{2}^-$	3181	7	12	37.86 (partition 1)	43.82 (partition 1)
$\frac{19}{2}^-$	3818	7	12	61.42 (partition 1)	69.33 (partition 1)
$\frac{21}{2}^-$	5564	7	16	57.92 (partition 1)	63.95 (partition 1)
$\frac{23}{2}^-$	5714	7	16	66.52 (partition 1)	72.65 (partition 1)
$(\frac{25}{2})^-$	8492	13	12	24.57 (partition 2)	33.26 (partition 1)
$(\frac{27}{2})^-$	9299	15	12	39.64 (partition 2)	57.23 (partition 1)

TABLE V. Summary of the properties of the band-terminating state in ^{51}Cr.

Spin	E_x	τ (ps)		$B(E2)$ (e^2 fm^4)		Q_0 (e fm^2)	
$(\hbar)$	(keV)	Expt.	Theo.	Expt.	Theo.	Expt.	Theo.
$J^\pi = \frac{23}{2}^-$ $K^\pi = \frac{15}{2}^-$	5714.08(20)	0.42(5)	0.27	76.1(106)	77.4	89.01(622)	106.86

Shape	β_2	$B(M1)$ (μ_N^2)		g factors			
		Expt.	Theo.				
Noncollective prolate	0.25(2)	1.5(3)	0.8	$g = 0.72(16)$; $g_{SM} = 0.83$; $g_{emp} = 0.87$			

tion from $(f_{7/2})^{11}$ configuration, starting from the bandhead, reaches a peak value for the yrast $\frac{19}{2}^-$ state. Following this, it slightly falls for the yrast $\frac{21}{2}^-$ state and then finally attains its maximum value for the yrast $\frac{23}{2}^-$ band-terminating state. The peak value of the total percentage contribution from $(f_{7/2})^{11}$ configuration for the yrast $\frac{19}{2}^-$ state, as well as its slight fall for the yrast $\frac{21}{2}^-$ state, are well reflected both in the measured and calculated $B(E2)$ values with a dip followed by a slight up-bend (Fig. 13). However, further rise in the measured as well as calculated $B(E2)$ value for the yrast $\frac{23}{2}^-$ state cannot be explained here in terms of the total percentage contribution from $(f_{7/2})^{11}$ configuration. This may be due to the influence of the newly proposed $K^\pi = \frac{19}{2}^-$ sequence, which calls for further experimental and theoretical investigations.

Figure 13 shows the evolution of the square root of experimental $B(E2)$ values along the yrast states in ^{51}Cr. The square root of $B(E2)$ values are plotted as it is directly pro-

FIG. 13. Depiction of experimental $\sqrt{B(E2)}$ values as a function of twice the spin ($2J$) value along the yrast line in ^{51}Cr, and their comparison with those obtained following shell-model calculations. Experimental data from neighboring $f_{7/2}$ nuclei [3] are also plotted for comparison.

portional to the quadrupole deformation of the nucleus [4,22]. The calculated values for the same nucleus, as obtained from the LSSM calculations, are also plotted for comparison. It is evident that both the experimental and calculated values agree rather well up to the band-terminating state in this nucleus (Fig. 13). The square root of experimental $B(E2)$ values for the ^{49}Cr [34] and ^{45}Sc [35] nuclei along their yrast sequences are also compared in Fig. 13. The ^{49}Cr nucleus, having the same proton number but two fewer neutrons than ^{51}Cr, has higher $B(E2)$ values for its yrast states, thereby implying more collectivity. As for the ^{45}Sc and ^{51}Cr cross-conjugate nuclei, the experimental data clearly show that the $B(E2)$ values for the yrast states in ^{45}Sc with a dominant configuration of half-filled neutron $f_{7/2}$ orbital, and those in ^{51}Cr with a dominant configuration of half-filled proton $f_{7/2}$ orbital, are relatively much closer to each other. These observations suggest that the half-filled proton (neutron) orbital, coupled with a near-magic neutron (proton) orbital, drives the nucleus favorably toward a single-particle structure with low collectivity.

The reduced magnetic transition probabilities [$B(M1)$], calculated for the yrast states using LSSM calculations, have been found to be in good agreement with the experimental values as shown in Table II. The g factors, obtained from LSSM calculations in the present work have also been compared with the g factors deduced from the experimental $B(M1)$ values (Table III) and have been found to be in good agreement. Furthermore, the empirical g factors for the yrast states were deduced using the formula:

$$g_{emp} = \frac{\mu}{I} = \frac{1}{I}[g_p(I_{p1} + I_{p2} + \cdots) + g_n(I_{n1} + I_{n2} + \cdots)],$$
(9)

considering $g_p = 1.38$ and $g_n = -0.30$, as prescribed by Brandolini *et al.* [4]. Thus, the empirical g factor, for example, for the $\frac{23}{2}^-$ band-terminating state, turns out to be $g = \mu/I = 2/23[1.38\,(7/2 + 5/2 + 3/2 + 1/2) - 0.3\,(7/2)] = 0.87$. The empirical g factors have also been found to be in fair agreement with both the experimental and shell-model-predicted g factors. It is to be noted that the magnetic properties of the anticipated $K^\pi = (\frac{19}{2}^-)$ sequence have not been addressed in the present work. More experimental data are required to have an unambiguous K value of this newly proposed sequence of states and a complete picture of their magnetic properties.
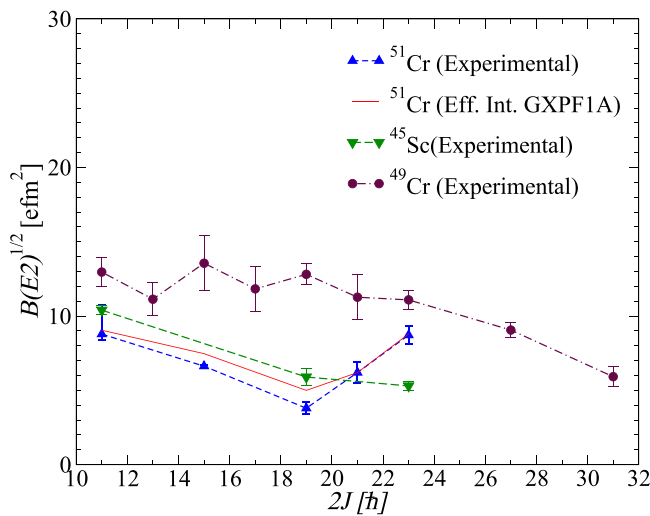
V. SUMMARY

In summary, a dedicated measurement employing heavy-ion-induced reaction and a high-efficiency clover detector array (INGA) has been carried out to investigate the higher-spin states in the ^{51}Cr nucleus. This happens to be the first instance when using a heavy-ion-induced reaction, the states in the previously reported $K^{\pi} = \frac{1}{2}^{-}$ strongly deformed band have been observed in this nucleus. The $K^{\pi} = \frac{7}{2}^{-}$ ground-state band and $K^{\pi} = \frac{15}{2}^{-}$ three-quasiparticle band have now been extended to higher excitation energies with the observation of new γ transitions. The yrast sequence in the $K^{\pi} = \frac{15}{2}^{-}$ band, in particular, has been extended beyond band termination, up to an excitation energy of $E_x \approx 9.3$ MeV. The present investigation has succeeded in identifying the previously anticipated, however unobserved, side-feeding transitions to the yrast states. DCO and polarization measurements have rendered unambiguous spin-parity assignments to multiple yrast states having tentative assignments previously. Unambiguous lifetime measurements for the yrast states in the $K^{\pi} = \frac{15}{2}^{-}$ band, up to and beyond the band-terminating state, have been carried out for the first time in this nucleus following analysis of distinct Doppler-broadened line shapes. The reduced $E2$ and $M1$ transition rates were deduced for the yrast sequence, and the intrinsic quadrupole moments, deformation parameters (β_2), and the g factors were extracted from those values. Following systematic observation of the profile of $B(E2)$ values along the yrast line in the neighboring nuclei, it has been argued that the half-filled proton (neutron) orbital, coupled with a near-magic neutron (proton) orbital, favorably drives a nucleus like ^{51}Cr toward single-particle structure with lesser collectivity. The shell-model calculations were carried out in the full fp valence space outside a ^{40}Ca core, with no restrictions imposed on the number of valence particles excited to the levels above $1f_{7/2}$. Overall, the experimental level energies, lifetimes, reduced transition probabilities, and g factors were found to be in good agreement with the LSSM calculations. It is inferred that the ^{51}Cr nucleus is prolate deformed at lower spins in its yrast sequence and becomes oblate at $\frac{21}{2}^{-}$, which then turns into a noncollective prolate shape at band termination. At the highest observed spin in the yrast structure, this nucleus again becomes an oblate deformed structure. Thus, the present investigation renders a detailed account of the level scheme of ^{51}Cr nucleus, which is, by far, the most enriched one to date following a heavy-ion-induced reaction. Nevertheless, it would be interesting to study the character of the newly proposed $K^{\pi} = (\frac{19}{2}^{-})$ sequence, its further evolution to higher spins, and interplay with the $K^{\pi} = \frac{15}{2}^{-}$ yrast band.

[1] M. A. Bentley, C. D. O'Leary, A. Poves, G. Martínez-Pinedo, D. E. Appelbe, R. A. Bark, D. M. Cullen, S. Ertürk, and A. Maj, Phys. Lett. B **437**, 243 (1998).

[2] J. A. Cameron, D. G. Popescu, and J. C. Waddington, Phys. Rev. C **44**, 2358 (1991).

[3] J. Wang and X. Huang, Nucl. Data Sheets **144**, 1 (2017).

[4] F. Brandolini and C. A. Ur, Phys. Rev. C **71**, 054316 (2005).

[5] I. M. Szoghy, J. S. Forster, and G. C. BalL, Nucl. Phys. A **201**, 433 (1973).

[6] J. Kasagi and H. Onhuma, J. Phys. Soc. Jpn. **45**, 1099 (1978).

[7] Z. P. Sawa, J. Blomqvist, and W. Gullholmer, Nucl. Phys. A **205**, 257 (1973).

[8] J. Kasagi and H. Onhuma, J. Phys. Soc. Jpn. **48**, 351 (1980).

[9] D. K. Avasthi, K. C. Jain, and I. M. Govil, Acta Phys. Polon. B **16**, 847 (1985).

[10] R. Palit, S. Saha, J. Sethi, T. Trivedi, S. Sharma, B. S. Naidu, S. Jadhav, R. Donthi, P. B. Chavan, H. Tan, and W. Hennig, Nucl. Instrum. Methods A **680**, 90 (2012).

[11] D. C. Radford, Nucl. Instrum. Methods A **361**, 297 (1995).

[12] https://radware.phy.ornl.gov

[13] J. Wells and N. Johnson, Oak Ridge National Laboratory, Report No. ORNL-6689, 1991 (unpublished).

[14] https://digital.library.unt.edu/ark:/67531/metadc1070831/m2/1/high_res%_d/5226283.pdf.

[15] A. Krämer-Flecken, T. Morek, R. M. Lieder, W. Gast, G. Hebbinghaus, H. M. Jäger, and W. Urban, Nucl. Instrum. Methods A **275**, 333 (1989).

[16] https://www-nds.iaea.org/public/ensdf_pgm/.

[17] K. Starosta et al., Nucl. Instrum. Methods A **423**, 16 (1999).

[18] P. M. Jones, L. Wei, F. A. Beck, P. A. Butler, T. Byrski, G. Duchêne, G. de France, F. Hannachi, G. D. Jones, and B. Kharraja, Nucl. Instrum. Methods A **362**, 556 (1995).

[19] S. K. Saha, M. Maynard, and B. C. Robertson, Nucl. Phys. A **339**, 253 (1980).

[20] R. Chakrabarti et al., Proc. DAE Symp. Nucl. Phys. **65**, 62 (2021).

[21] J. F. Ziegler, J. P. Biersack, and U. Littmark, *The Stopping and Range of Ions in Solids*, Stopping and Ranges of Ions in Matter, Vol. 1, edited by J. F. Ziegler, J. P. Biersack, and U. Littmark (Pergamon, New York, 1985).

[22] S. Mukhopadhyay et al., Nucl. Phys. A **1000**, 121785 (2020).

[23] A. Görgen, J. Phys. G: Nucl. Part. Phys. **37**, 103101 (2010).

[24] F. B. Malikand W. Scholz, Phys. Rev. **150**, 919 (1966).

[25] D. G. Sarantitesand W. G. Winn, Nucl. Phys. A **155**, 257 (1970).

[26] A. Poves, J. Sánchez-Solano, E. Caurier, and F. Nowacki, Nucl. Phys. A **694**, 157 (2001).

[27] R. Chakrabarti and S. Mukhopadhyay, Proc. DAE Symp. Nucl. Phys. **63**, 354 (2018).

[28] M. Honma, T. Otsuka, B. A. Brown, and T. Mizusaki, Eur. Phys. J. A **25**, 499 (2005).

[29] A. Poves and A. Zuker, Phys. Rep. **70**, 235 (1981).

[30] W. A. Richter, M. G. Van Der Merwe, R. E. Julies, and B. A. Brown, Nucl. Phys. A **523**, 325 (1991).

[31] B. A. Brown and W. D. M. Rae, Nucl. Data Sheets **120**, 115 (2014).

[32] R. du Rietz, S. J. Williams, D. Rudolph, J. Ekman, C. Fahlander, C. Andreoiu *et al.*, Phys. Rev. C **72**, 014307 (2005).

[33] A. V. Afanasjev, D. B. Fossan, G. J. Lane, and I. Ragnarsson, Phys. Rep. **322**, 1 (1999).

[34] F. Brandolini *et al.*, Nucl. Phys. A **693**, 517 (2001).

[35] P. Bednarczyk *et al.*, Eur. Phys. J. A **2**, 157 (1998).